Int J Adv Manuf Technol (2016) 85:2715–2728
DOI 10.1007/s00170-015-8142-7

ORIGINAL ARTICLE

Comprehensive thermal compensation of the servo axes of CNC machine tools

Kuo Liu[1] · **Yu Liu**[2] · **Mingjia Sun**[3] · **Yuliang Wu**[3] · **Tiejun Zhu**[3]

Received: 30 July 2015 / Accepted: 13 November 2015 / Published online: 24 November 2015

Abstract The disadvantages of the common thermal error compensation methods were analyzed. Based on the analysis, we report the concept of the comprehensive thermal error (CTE) of the servo axes of CNC machine tool. The total CTE was divided into the thermal expansion error (TEE) in the stroke range and the thermal drift error (TDE) of origin, and their sources and effects on workpieces were analyzed. Furthermore, models for TEE and TDE were established. The model for TEE derived from the heat production, conduction, and convection theory predicted the thermal field of a screw and the thermal errors of servo axes in real time. The model for TDE was established by the multiple linear regression method. The experiments were carried out on a vertical machining center. The simulation and experimental results indicate that a high accuracy stability can be achieved with error compensation, even when the moving state is changed. To visualize the effect of error compensation with naked eyes, a special machining process was designed for a rectangular workpiece. The machining results confirm that the proposed models provide a high accuracy stability and robustness.

Keywords CNC machine tools · Comprehensive thermal error · Thermal expansion error · Thermal drift error · Compensation

✉ Kuo Liu
liukuo0727@qq.com

[1] College of Mechanical Science and Engineering, Jilin University, Changchun 130025, People's Republic of China

[2] College of Mechanical Engineering and Automation, Northeastern University, Shenyang 110819, People's Republic of China

[3] State Key Laboratory, Shenyang Machine Tool (Group) Co., Ltd, Shenyang 110142, People's Republic of China

1 Introduction

Thermal error is an important factor for the accuracy stability of CNC machine tools. Several experiments show that thermal errors account for 40–70 % of the total error of machine tools [1–3]. Thermal errors can be minimized mainly by two methods: error prevention and compensation [4, 5]. The error prevention method can eliminate or reduce the deformation of machines during the design or construction phase of machine tools, such as symmetric design and screw/nut cooling. However, these methods have some disadvantages: (1) Symmetric design is a good method for controlling thermal errors. However, only a specific axis can be designed as a heat symmetric structure, such as the *y*-axis of gantry machine tools, and the applications of heat symmetric structures are limited. (2) A higher cost of screw/nut cooling. For example, the costs of screw DKFZ4016TR-5-P3/1414X1159-D1 manufactured by China Nanjing Technical Equipment Manufacture Co., Ltd. with and without cooling are $480 and $275, respectively. When the cost of a cooling machine (for example, the price of cooling machine of Taiwan KAUKAN Co., Ltd. is approximately $6500) is added, the cost of the machine tool increases significantly. Moreover, the start of the cooling machine is intermittent, causing the fluctuation inaccuracy. Thus, error prevention is not an economical or widely used method for controlling thermal errors.

Error compensation method creates an opposite error to eliminate the original thermal error [6–8]. Error compensation method has many advantages such as a lower cost and diverse applications. Thermal error compensation techniques have been widely investigated. Feng et al. [9] reported a mathematical model for the transient temperature of a screw with respect to time. To solve the problem of uneven heat distribution on a screw shaft, the screw shaft was divided into several evenly distributed heat regions. Six test pieces were machined; the

results indicate that the accuracy of the pieces significantly improved than that obtained without error compensation. Fan et al. [10] proposed an error model based on orthogonal polynomials to improve the machining accuracy of a CNC machine; the thermally induced spindle and geometric error was compensated by 90 % than that without compensation. Wu et al. [11] suggested a model to compensate thermal expansion error by multivariable regression analysis. Based on the simulation, the number of sensors was reduced from 10 to 6. Zhang et al. [12] determined an optimal threshold to optimize the temperature variable in thermal error modeling. Pajor et al. [13] suggested a novel system that facilitates a continuous compensation of the thermal deformations of a screw during its work under workshop conditions. Zhang et al. [14] proposed a novel modeling method for machine tool thermal error, combining the advantages of both the grey model and artificial neural network (ANN) in terms of data processing.

Studies show that the aforementioned compensation methods suffer from the following disadvantages: (1) They only work under specific conditions. (2) Many temperature sensors are required to achieve a high accuracy, thus increasing the cost significantly. Moreover, one temperature sensor should be placed on the moving nut in many of the aforementioned methods, easily causing failure. (3) The methods have a poor robustness [15]. When the moving position and speed in actual machining are different from those used in modeling, the predicted results are always poor. (4) Most importantly, most of the studies focused on thermal expansion error (TEE) in the stroke range of servo axis. The thermal drift error (TDE) of origin has been rarely studied.

In this study, the comprehensive thermal error (CTE) of a servo axis was divided into two parts: TEE in the stroke range and TDE of origin. According to the theoretical analysis, TEE is mainly caused by the variation in ambient temperature and the frictional heat of the screw. The screw in the stroke range was discretized, and based on the heat production, conduction, and convection theory, the temperature field of the screw and thermal errors of a servo axis were predicted in real time. TDE is mainly caused by (i) the temperature variation in the bearing block near the origin of a servo axis, (ii) the heat conduction of the screw in the stroke range, and (iii) ambient temperature variation. The multiple linear regression method was used for the prediction and compensation of TDE.

2 CTE of a servo axis

Most of the previous studies focused on TEE. The CTE of a servo axis can be divided into two parts: TEE E_e+E_m and TDE E_d, where E_e is the thermal error induced by ambient temperature variation and E_m is the thermal error induced by the frictional heat of the screw. Figure 1 shows the schematic drawing of CTE. Figure 2 shows the CTE decomposition diagram.

Figure 1 shows that when the worktable warms up in the range 0–P_x, the distance between the spindle and worktable changes due to thermal errors. On one hand, the ambient temperature variation and the frictional heat of the screw induce E_e and E_m. On the other hand, the distance between the origin of servo axis and spindle changes. Because of the heat of bearing block, heat conduction from the screw in the stroke range, and ambient temperature variation, E_d appears in the distance between the origin of servo axis and spindle. Figure 2 shows that CTE is the sum of TEE and TDE. TEE depends on the position and temperature, and TDE does not depend on the position.

TDE cannot be discovered in a commonly positioning error test, because the clearance at the test starting point is essential in a commonly positioning error test using a laser interferometer [16]. Therefore, the tested positioning errors at the test starting point are always zero. However, in fact, E_d exists and significantly affects workpieces. Figure 3 shows the effects of TEE and TDE on workpieces.

Figure 3 shows that the first workpiece is machined after the tool setting, and the distance between the two milled holes is L. When the nth workpiece is machined without tool setting, when only TDE exists, the two holes drift E_d in the same direction, and the distance between the two milled holes is still L. When only TEE exists, the distance between the two milled holes is $L+E_e+E_m$.

3 Modeling and parameter optimization

3.1 TEE

3.1.1 Model of TEE

The thermal field of a screw is the function of position and temperature [17]. The screw was simplified to a one-dimensional bar because only the axial thermal deformation of screw affects the machining accuracy [18]. The screw in the stroke range was discretized into M segments, and the length of each segment was L. Moreover, the length of screw outside the stroke range in the motor side was set as L_{m0}, and the length of the screw outside the stroke range in the other side was set as L_{m1}, as shown in Fig. 1.

3.2 Error caused by ambient temperature variation

In general, the change in ambient temperature is slow, and the change in the temperature of the screw caused

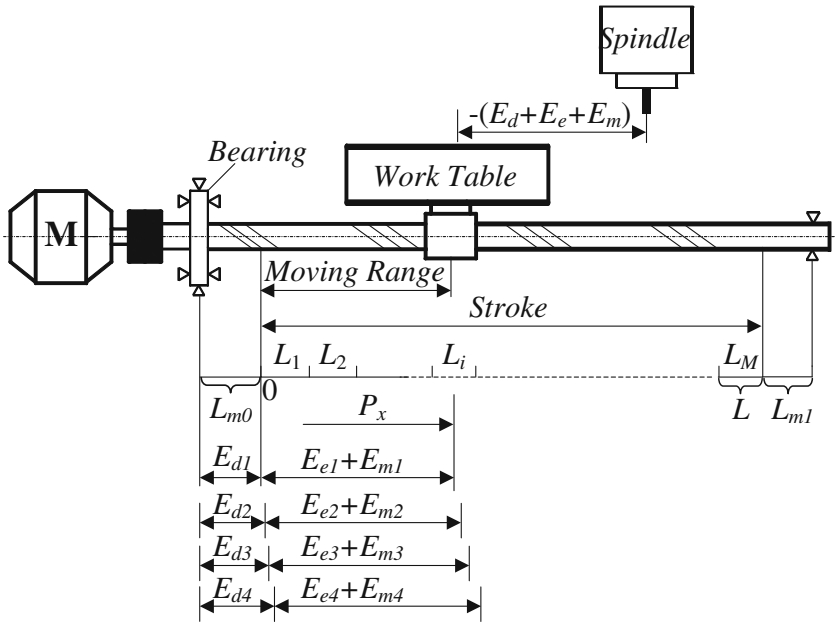

Fig. 1 Schematic drawing of CTE

by ambient temperature variation is slow. Thus, the error E_e caused by ambient temperature variation in the stroke range can be expressed as follows:

$$E_e = \alpha \times (T_b - T_{b0}) \times P_x \tag{1}$$

where α is the thermal expansion coefficient of the screw, μm/(m×°C); T_b is the real-time ambient temperature, °C; T_{b0} is the initial ambient temperature, °C; and P_x is the real-time position, mm.

3.3 Error caused by movement

For a certain segment L_i of a screw in the stroke range, the frictional heat increases the temperature of L_i. L_i conducts heat to both sides of L_i and simultaneously exchanges the heat with the surrounding air. Therefore, the thermal equilibrium equation for L_i can be expressed as follows:

$$cm\Delta T_{L_i} = Q_{L_i-1} - Q_{L_i-2} - Q_{L_i-3} \tag{2}$$

where m is the mass of a segment of the screw, kg; c is the heat capacity of the screw, J/(Kg×°C); ΔT_{L_i} is the temperature rise of L_i, °C; Q_{L_i-1} is the frictional heat production of L_i, J; Q_{L_i-2} is the axial heat conduction of L_i to both the sides, J; and Q_{L_i-3} is the heat convection of L_i with the surrounding air, J.

3.4 Frictional heat production

For L_i, the total frictional heat production $Q_{L_i}-1$ can be expressed as follows:

$$Q_{L_i-1} = Q \times N \tag{3}$$

where Q is the heat production of L_i after one friction, J; and N is the number of frictions of L_i.

3.5 Axial heat conduction

The heat passing through the screw cross section in unit time is directly proportional to the change in temperature and the cross-sectional area of the screw:

$$Q_{L_i-2} = \alpha \times A \times \frac{\partial T}{\partial x} = A \times q' \tag{4}$$

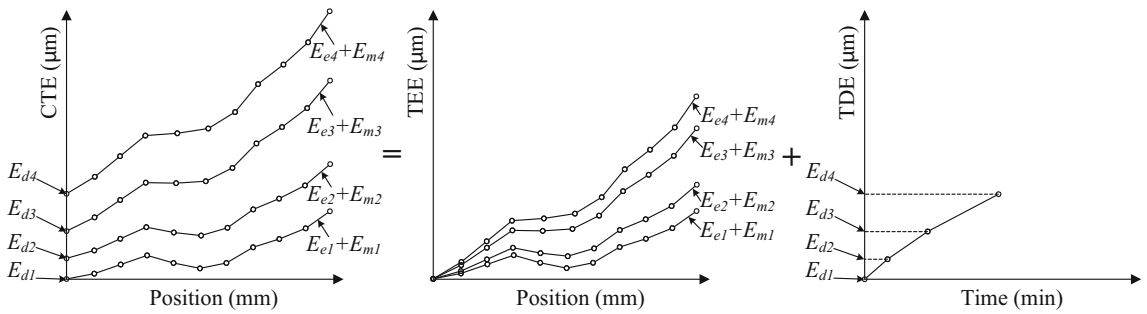

Fig. 2 CTE decomposition diagram

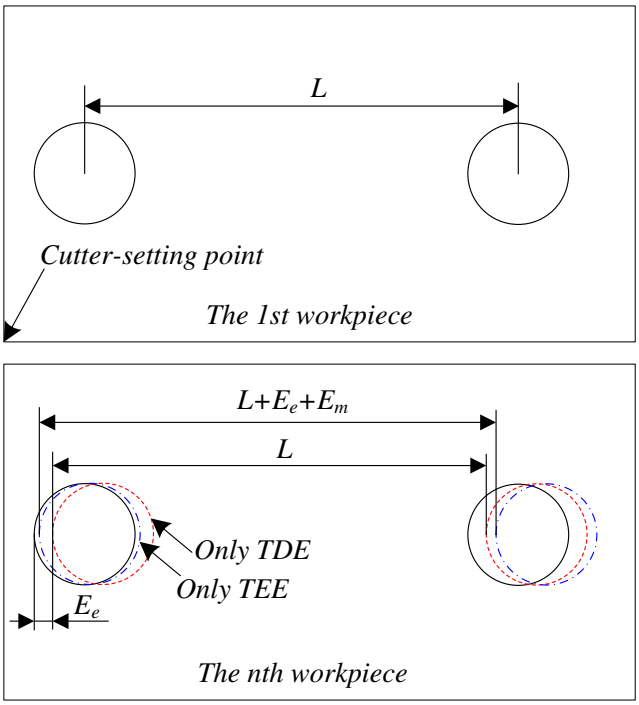

Fig. 3 Effects of TEE and TDE on workpieces

where A is the cross-sectional area of the screw, m^2; and q' is the density of heat flow, J/m^2.

After discretizing Eq. (4) and supposing that the nut moves on L_i at time t, the axial heat conduction $Q_{L_i}{-}2$ during (t, $t+\Delta t$) can be expressed as follows:

$$Q_{L_i-2} = \alpha \times A \times \frac{(T_{L_i}-T_{L_{i-1}}) + (T_{L_i}-T_{L_{i+1}})}{L} \times \Delta t \tag{5}$$

where T_{L_i} is the temperature of L_i at a certain time, °C; $T_{L_{i-1}}$ is the temperature of L_{i-1} at a certain time, °C; and $T_{L_{i+1}}$ is the temperature of L_{i+1} at a certain time, °C.

In particular, for L_1 and L_M

$$Q_{L_1-2} = \alpha \times A \times \frac{T_{L_1}-T_{L_0}}{L_{m0}} \times \Delta t + \alpha \times A \times \frac{T_{L_1}-T_{L_2}}{L} \times \Delta t \tag{6}$$

$$Q_{L_M-2} = \alpha \times A \times \frac{T_{L_M}-T_{L_{M-1}}}{L} \times \Delta t + \alpha \times A \times \frac{T_{L_M}-T_{L_{M+1}}}{L_{m1}} \times \Delta t \tag{7}$$

3.6 Heat convection

If the nut moves on L_i at time t, then the heat convection $Q_{L_i}{-}3$ during time (t, $t+\Delta t$) can be expressed as follows:

$$Q_{L_i-3} = h \times S \times (T_{L_i}-T_f) \times \Delta t \tag{8}$$

where h is the heat exchange coefficient [19], $W/(m^2 \times °C)$; S is the heat exchange area of L_i, $S \approx A \times L$, m^2; and T_f is the ambient temperature and almost the same as T_b, °C.

The heat exchange coefficient h can be affected by many factors, and according to Nusselt criterion, h can be expressed as follows:

$$h = \frac{N_u \times \lambda_a}{D} \tag{9}$$

where N_u is the Nusselt number; D is the feature size, m; and λ_a is the heat conduction coefficient of air, $W/(m \times °C)$.

The Nusselt number N_u under natural convection conditions can be expressed as follows:

$$N_u = C(G_r \times P_r)^m \tag{10}$$

where C and m are the coefficients and determined by the heat source and airflow [20], P_r is the Prandtl number, and G_r is the Grashof number:

$$G_r = \frac{gL^3\beta\Delta T}{\upsilon^2} \tag{11}$$

where g is the gravitational acceleration, m/s^2; β is the expansion coefficient of air, $°C^{-1}$; υ is the kinematic viscosity of air, m^2/s; and ΔT is the temperature difference between air and screw, °C.

The real-time temperature variation $\Delta T_{L_i}(t)$ of L_i can be obtained from Eqs. (3), (5), (6), (7), and (8).

The temperature variation of a screw is a dynamic process. Therefore, the temperature field of a screw also changes dynamically. For L_i, $T_{L_i}(t+\Delta t)$ at time $t+\Delta t$ can be calculated using $T_{L_i}(t)$ at time t [21]:

$$T_{L_i}(t+\Delta t) = T_{L_i}(t) + \Delta T_{L_i}(t) \tag{12}$$

Equation (12) shows that if the initial temperature T_{b0} of a screw in the thermal steady state is known, the entire thermal field $T_{L_i}(t)$ of the screw after any movement can be predicted.

The thermal errors E_m of a screw caused by the movement at a certain time t can be expressed as follows:

$$E_m = \sum_{i=1}^{M} \alpha \times (T_{L_i}-T_b) \times L_i \tag{13}$$

3.7 Calculation of TEE

The TEE E_{em} of a servo axis in the stroke range can be obtained from Eqs. (1) and (13):

$$E_{em} = E_e + E_m \tag{14}$$

Because the model for TEE records the dynamic process of the thermal field of a screw, the robustness of the model is very strong. Although the moving state of a servo axis changes, including the moving speed, moving range, and whether moving or not, excellent compensation effect can be obtained.

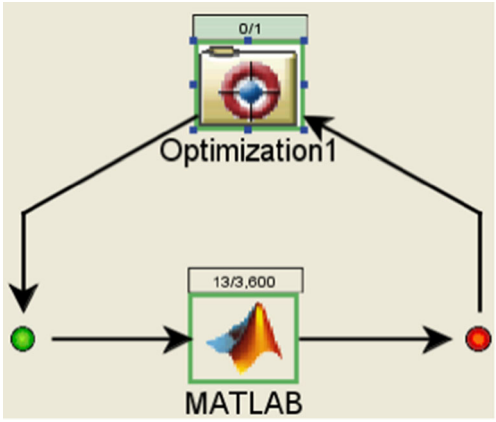

Fig. 4 Frame of automatic parameter optimization

3.8 Parameter optimization

In the model shown in Sect. 3.1.1, some parameters are difficult to determine, such as the coefficient of heat conduction α, heat capacity c, heat exchange coefficient h, heat production of L_i after one friction Q, the length of screw outside the stroke range in the motor side L_{m0}, and the length of screw outside the stroke range in the other side L_{m1}. For example, Eqs. (9), (10), and (11) show that the calculation of h is very complex and inaccurate. Thus, a parameter identification method is required to determine these parameters.

ISIGHT is an automatic parameter identification platform. This platform organizes the parameter identification process into a uniform frame [22, 23]. The program for optimization is written in MATLAB, and the Δ in Eq. (15) is set as the optimization objective function:

$$\Delta = \sum_{n=1}^{K} \sum_{m=1}^{J} (Et_{nm} - Ec_{nm}) \tag{15}$$

where Et_{nm} is the tested thermal error of the mth test point during the nth test; Ec_{nm} is the calculated thermal error of the mth test point during the nth test; K is the total test times; and J is the total test points of a servo axis.

Fig. 5 Test of thermal errors using a laser interferometer

MATLAB was added to ISIGHT as shown in Fig. 4, and the program for optimization, initial value of parameters, and upper and lower limits of the parameters were set. The above mentioned parameters were optimized using a pointer automatic optimizer.

3.9 TDE

According to the analysis shown in Sect. 2, TDE is mainly relative to the temperature variation ΔT_{br} of the bearing block near the origin of servo axis, the temperature variation ΔT_{L_1} of L_1 near the origin of servo axis, and ambient temperature

Table 1 Parameters of thermal tests

Axis	Number	Speed (mm/min)	Range (mm)	Time (min)
x	State 1	–	–	0
	State 2	5000	185–535	10
	State 3	5000	185–535	10
	State 4	5000	185–535	10
	State 5	5000	185–535	10
	State 6	5000	185–535	10
	State 7	5000	185–535	10
	State 8	0	171	10
	State 9	0	171	12
	State 10	0	171	11
	State 11	0	171	12
	State 12	0	171	15
y	State 1	–	–	0
	State 2	5000	−130 to −370	10
	State 3	5000	−130 to −370	10
	State 4	5000	−130 to −370	10
	State 5	5000	−130 to −370	10
	State 6	5000	−130 to −370	10
	State 7	5000	−130 to −370	9
	State 8	0	−490	7
	State 9	0	−490	9
	State 10	0	−490	9
	State 11	0	−490	10
	State 12	0	−490	10
z	State 1	–	–	0
	State 2	5000	−392 to −137	10
	State 3	5000	−392 to −137	10
	State 4	5000	−392 to −137	10
	State 5	5000	−392 to −137	10
	State 6	5000	−392 to −137	10
	State 7	5000	−392 to −137	8
	State 8	0	−10	10
	State 9	0	−10	10
	State 10	0	−10	10
	State 11	0	−10	12
	State 12	0	−10	10

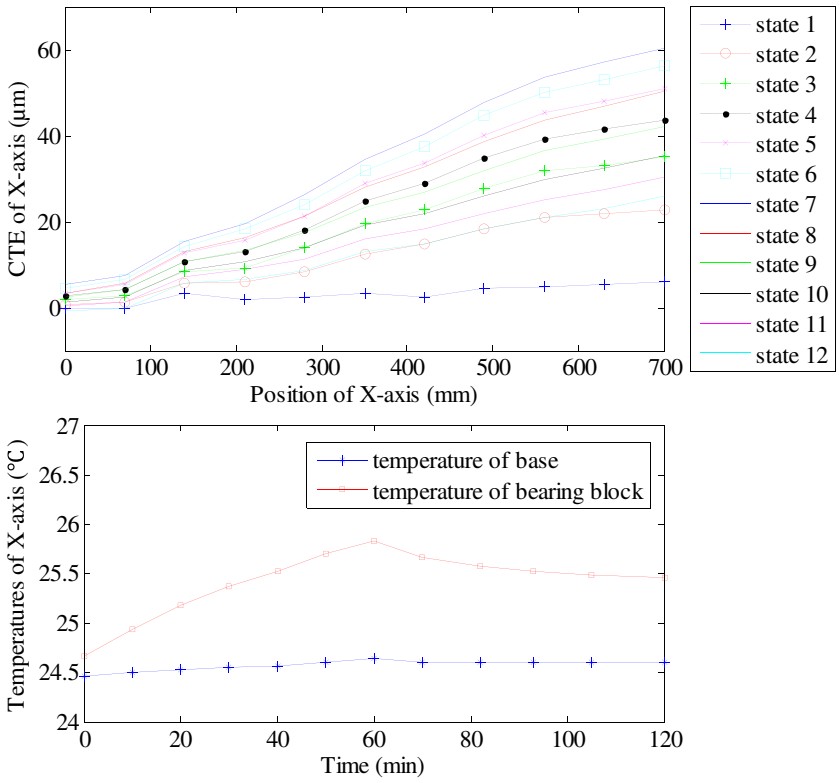

Fig. 6 Thermal errors and temperatures of *x*-axis

variation ΔT_b. In Fig. 1, the right direction close to the spindle was set as the forward direction in a commonly positioning error test. Thus, ΔT_{br} and ΔT_{L_1} move the worktable close to the spindle, and ΔT_b removes the worktable far away from the spindle. Supposing that E_d is linearly related to ΔT_{br}, ΔT_{L_1}, and ΔT_b, the model for E_d can be expressed as follows:

$$E_d = f(\Delta T_{br}, \Delta T_{L_i}, \Delta T_b) = a\Delta T_{br} + b\Delta T_{L_i} + c\Delta T_b + d \quad (16)$$

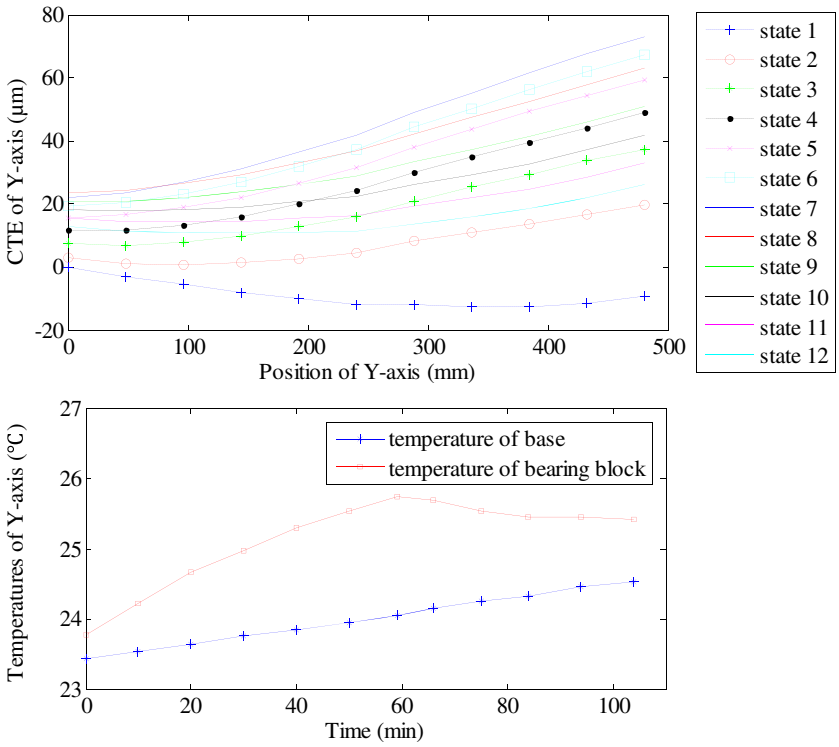

Fig. 7 Thermal errors and temperatures of *y*-axis

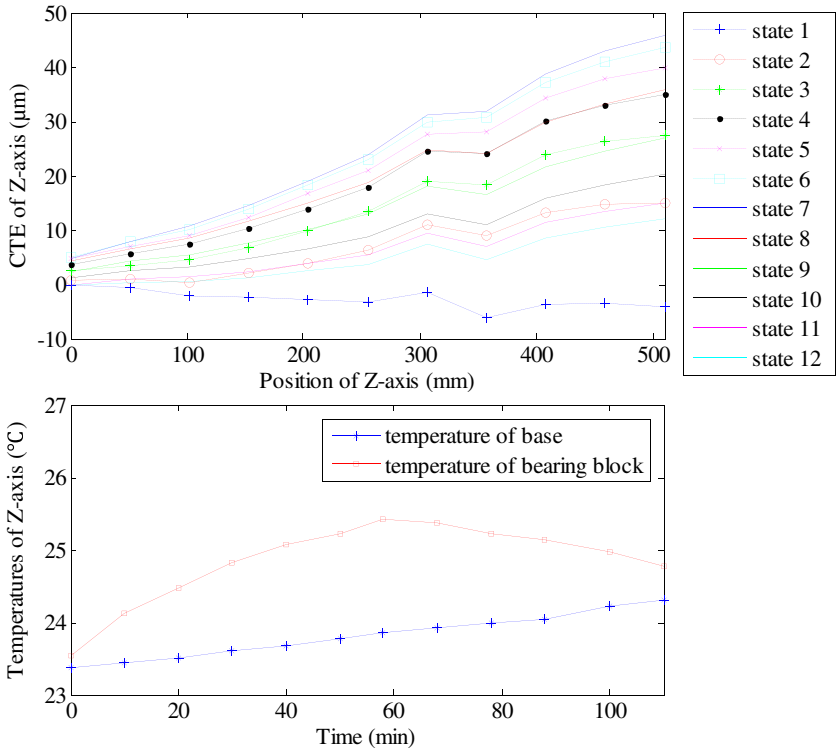

Fig. 8 Thermal errors and temperatures of *z*-axis

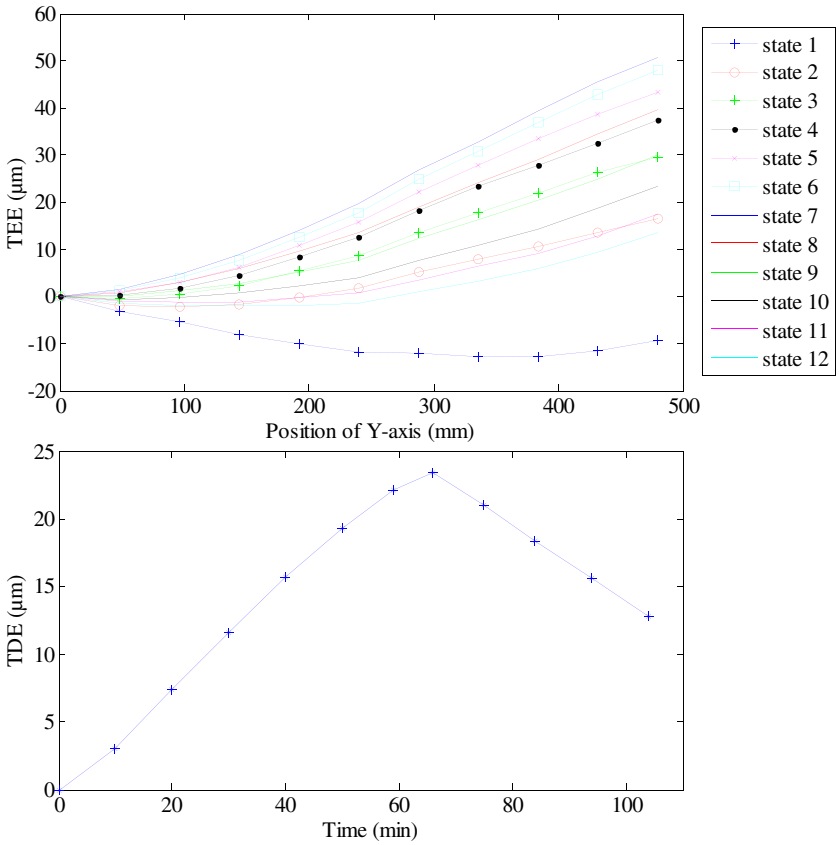

Fig. 9 CTE decomposition of *y*-axis: TEE and TDE

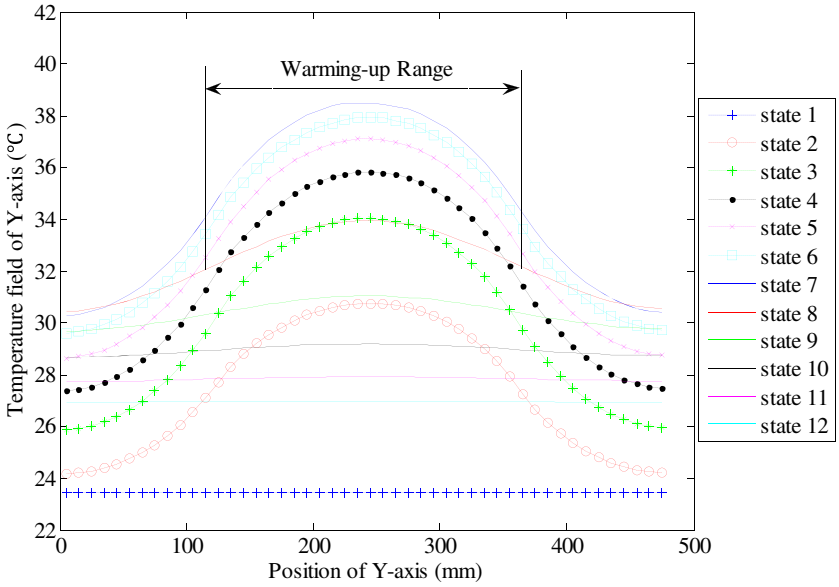

Fig. 10 Predicted temperature field of *y*-axis

where a, b, c, and d are the coefficients to be determined.

a, b, c, and d were solved by the least squares method, and the objective function and constraint condition can be expressed by Eq. (17).

$$\begin{aligned} &\min(Et_{\mathrm{d}}-Ec_{\mathrm{d}}) \\ &\quad a>0 \\ &s.t. \quad b>0 \\ &\quad c<0 \end{aligned} \tag{17}$$

3.10 Thermal error tests

The thermal error tests were carried out on a vertical machining center VMC850. FANUC 0*i*-MATE MD was used as the control system, and the maximum speeds of *x*-, *y*-, and *z*-axes were 32, 32, and 30 m/min, respectively. All these three axes are half-closed-loop control type without cooling, with screws fixed on one end and supported on the other end.

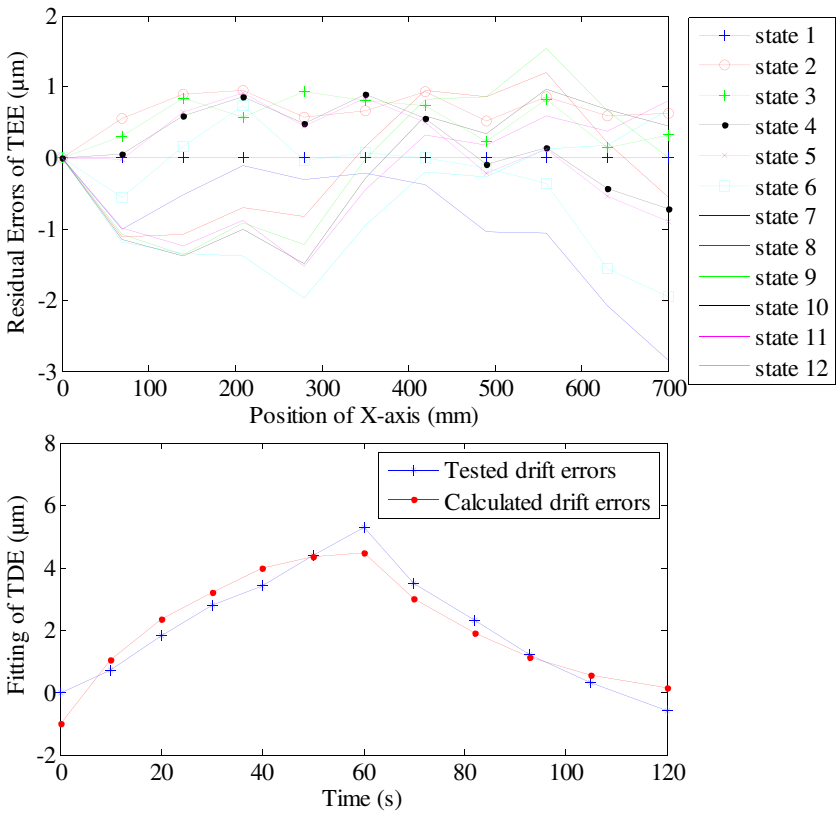

Fig. 11 Simulation of *x*-axis

Fig. 12 Simulation of *y*-axis

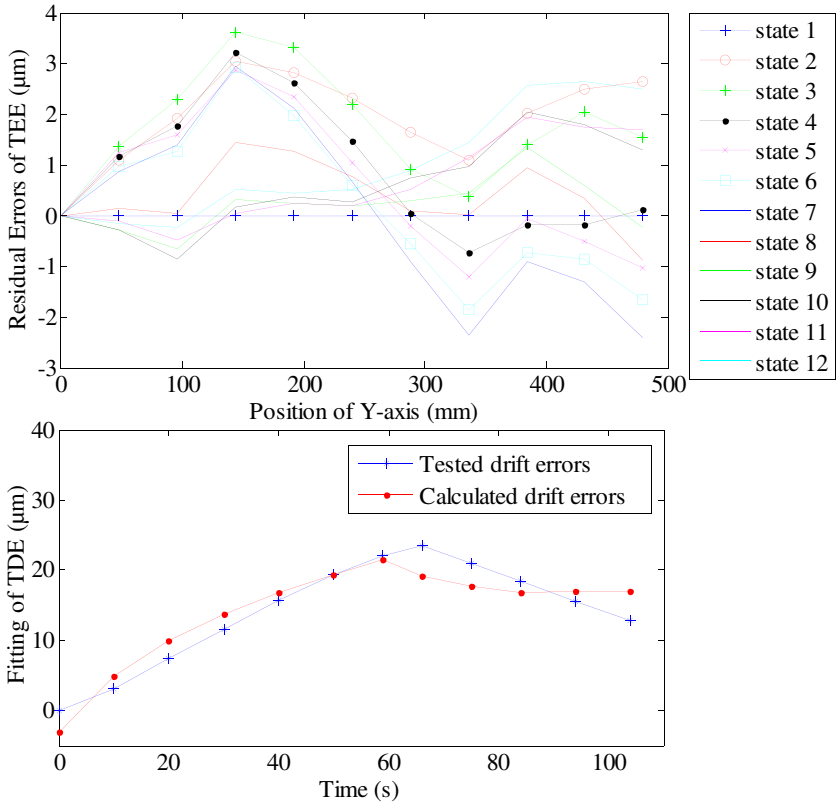

Six temperature sensors, with an accuracy of ±0.1 °C (5–45 °C), were placed on the bearing blocks near the origins and the bases near the screws of *x*-, *y*-, and *z*-axes. The thermal errors were tested using a dual-frequency laser interferometer

Fig. 13 Simulation of *z*-axis

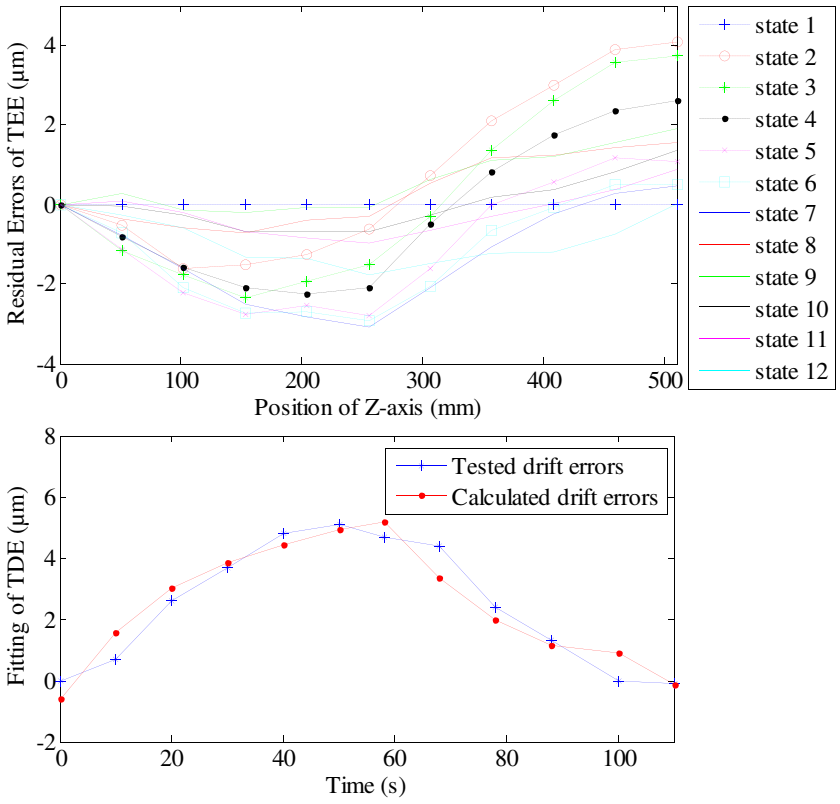

XL80. Importantly, the "expansion compensation of material" should be set as 20 °C to achieve the actual accuracy in any temperature instead of the accuracy after conversion at 20 °C. The investigation of thermal errors is shown in Fig. 5.

Taking the *y*-axis as an example, the procedure of the thermal test can be described as follows:

1. Test the initial positioning error of *y*-axis in the range from −10 to −490 mm, and record the values of the temperature sensors. Clearance at the test starting point was executed only in the first test.
2. Let the *y*-axis move in the range from −130 to −370 mm at a speed of 5000 mm/min for a period of time.
3. Stop the movement. Test the positioning error, and record the values of the temperature sensors.
4. Repeat steps (2) and (3) until the *y*-axis reaches the heat balance.
5. Stop the *y*-axis at −490 mm position to cool down. Test the positioning error at intervals, and record the values of the temperature sensors.

The thermal errors of the *x*- and *z*-axes were tested in the same manner. The test parameters of these three axes are shown in Table 1.

Figures 6, 7, and 8 show the test results of the *x*-, *y*-, and *z*-axes.

Figures 6, 7, and 8 show that the positioning errors at all the test points changed with time, including the positioning errors at the test starting point. Thus, the CTE was decomposed as follows: The thermal error data of all the tests were processed to make the errors at the first test points as zero, and the TEE was obtained. The errors at the first test points of all the tests were extracted to compose TDE. Taking the *y*-axis as an example, the CTE decomposition of the *y*-axis is shown in Fig. 9.

The TDE curve in Fig. 9 shows that in the warming-up phase, TDE increased because both the temperatures of the bearing block near the origin and L_1 segment near the origin increased; in the cooling-down phase, the TDE decreased because both the temperatures of the bearing block near the origin and L_1 segment near the origin decreased.

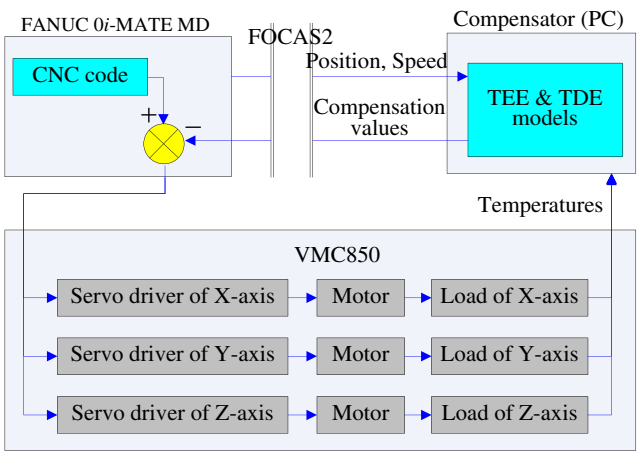

Fig. 14 Compensation principle

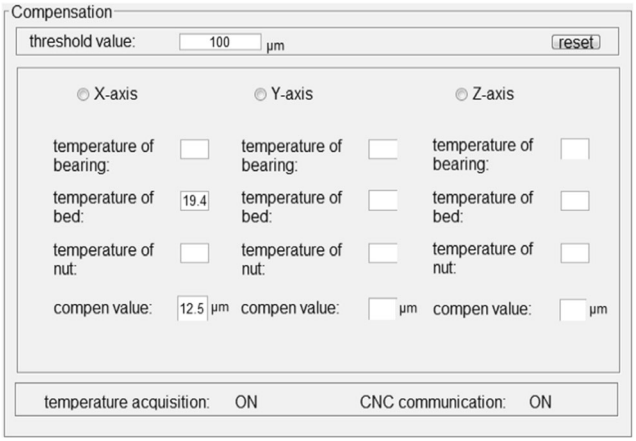

Fig. 15 Interface of thermal compensation software

The TEE and TDE of the *x*- and *z*-axes were obtained in a similar manner.

3.11 Verification

3.11.1 Simulation

The parameters were optimized following the procedure described in Sect. 3.1.2 using the data shown in Figs. 6, 7, and 8. The screws of *x*-, *y*, and *z*-axes were segmented according to $L=10$ mm; therefore, the screws of *x*-, *y*, and *z*-axes were discretized into 70, 48, and 51 segments, respectively.

Table 2 Parameters of thermal test

Axis	Number	Speed (mm/min)	Range (mm)	Time (min)
x	State 1	–	–	0
	State 2	8000	185–535	16
	State 3	5000	10–360	10
	State 4	7000	360–710	10
	State 5	0	10	10
y	State 1	–	–	0
	State 2	5000	−370 to −130	10
	State 3	6000	−370 to −130	10
	State 4	7000	−490 to −250	12
	State 5	8000	−10 to −250	10
z	State 1	–	–	0
	State 2	5000	−137 to −392	10
	State 3	6000	−150 to −380	12
	State 4	7000	−120 to −410	10
	State 5	8000	−10 to −265	10

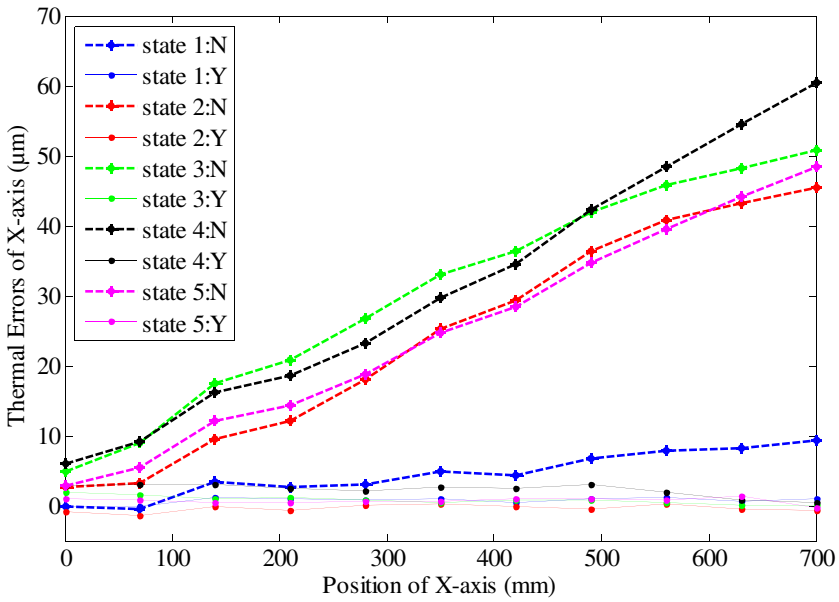

Fig. 16 Experimental results of *x*-axis

The model of TEE shown in Sect. 3 predicted the temperature field of a screw. Taking the *y*-axis as an example, after the parameters were optimized, the model well calculated the temperature of the *y*-axis of each screw segment at any point of time. Figure 10 shows the temperature field distribution of *y*-axis. In the warming-up phase (states 1–7), the temperature of the screw increased, and the maximum temperature was obtained in the middle of the warming-up range. In the free cooling-up phase (states 8–12), the temperature of the screw decreased, and the maximum temperature decrease was obtained in the middle of the warming-up range.

Based on the predicted temperature field of the screw, the thermal errors at any position and time were calculated using Eq. (13).

The simulation was carried out using Matlab R2014a, and the results are shown in Figs. 11, 12, and 13.

Figures 11, 12, and 13 show that the predicted results of TEE and TDE are very close.

3.12 Experimental

The communication between the thermal compensator and FANUC 0*i*-MATE MD was achieved through Ethernet [20]. Fanuc Open CNC API Specifications2 (FOCAS2)

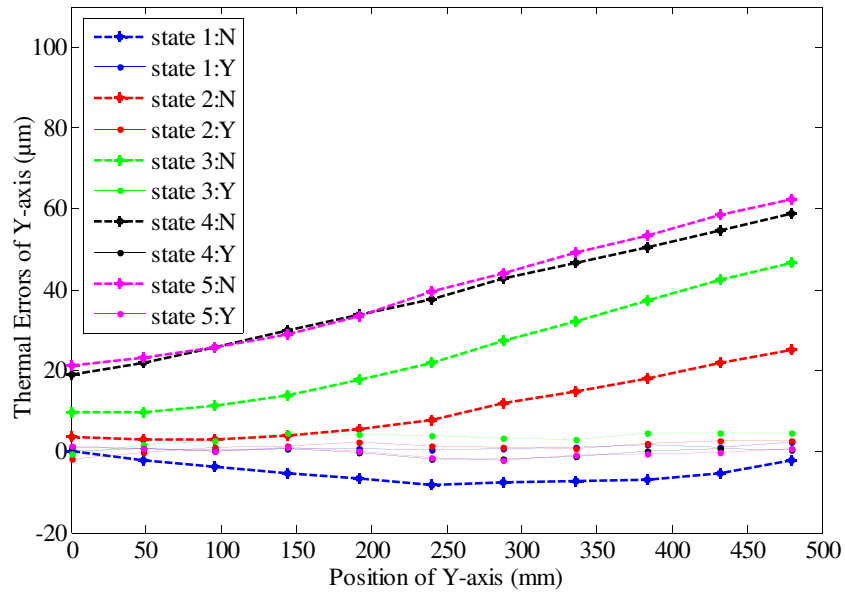

Fig. 17 Experimental results of *y*-axis

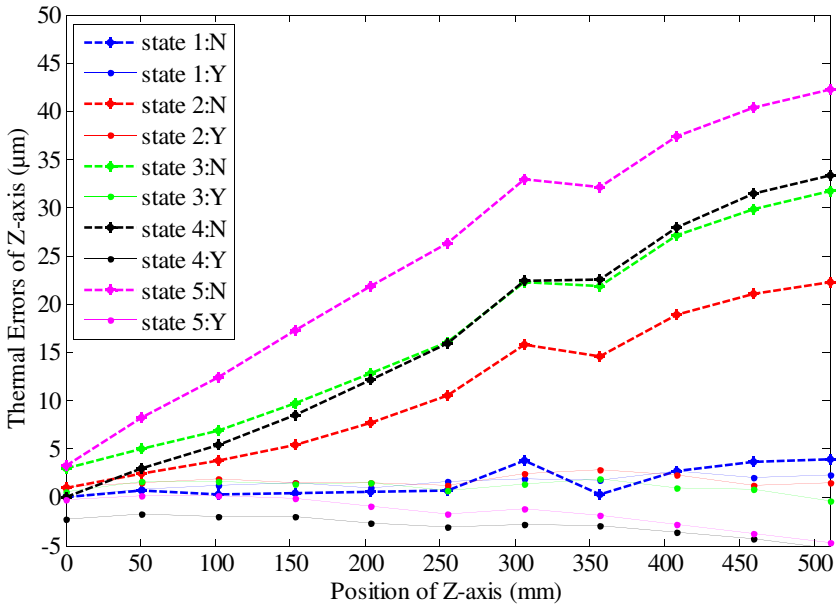

Fig. 18 Experimental results of *z*-axis

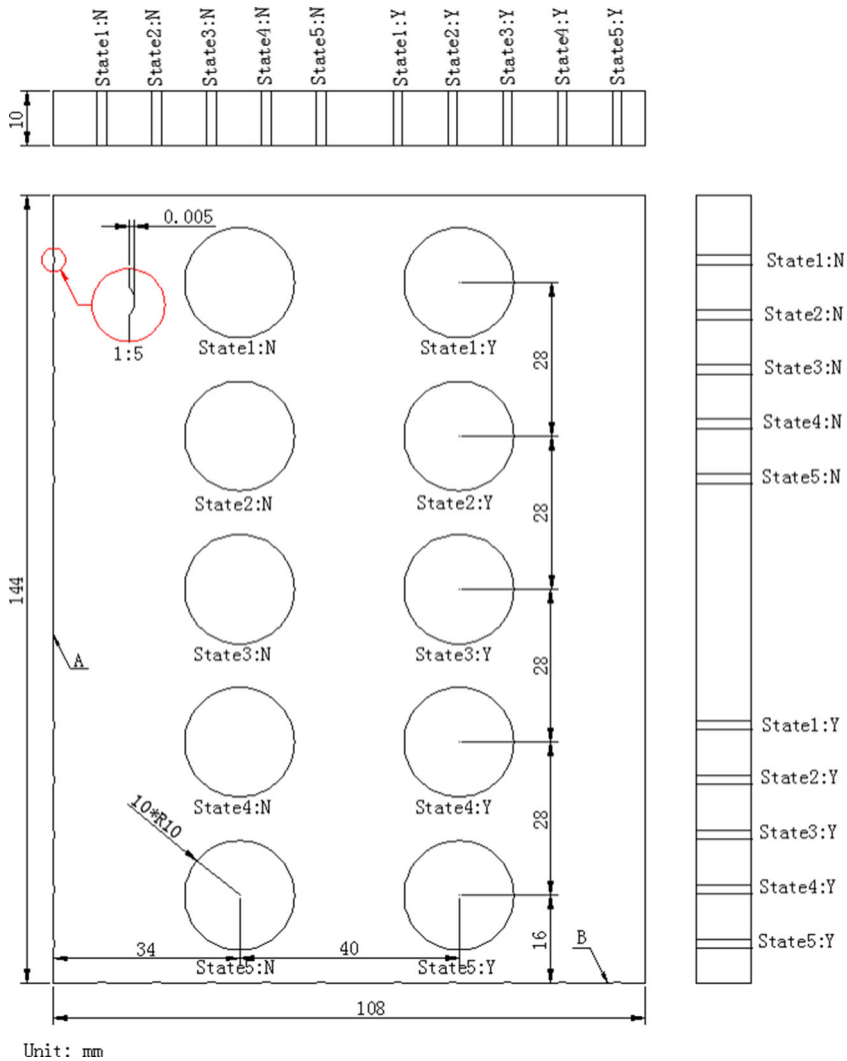

Fig. 19 Workpiece for verification

was used to obtain the reading of the positions of servo axes from CNC and the writing of the compensation values to CNC. The compensation principle is shown in Fig. 14.

The thermal test and compensation software were developed in MATLAB R2014a for thermal compensation experiments. The interface of thermal compensation is shown in Fig. 15.

Experiments were carried out using a laser interferometer according to the varying moving states shown in Table 2. For each time, first, a test without compensation was carried out, and then a test with compensation was carried out. Therefore, the residual errors before and after the compensation can be easily contrasted.

The experimental results are shown in Figs. 16, 17, and 18.

In Figs. 16, 17, and 18, "N" denotes the thermal errors without compensation and "Y" denotes the residual errors with compensation.

Figures 16, 17, and 18 show that the thermal errors without compensation are high and the thermal errors with compensation are very low. In particular, the moving information in Table 2, including the moving speed, moving range, and whether moving or not, changed; however, the residual errors after the compensation were always low. The high accuracy and strong robustness of the suggested model were verified again.

3.13 Machining

Before and after the compensation, machining was performed for further verification. A special workpiece was designed to observe the differences before and after the compensation with naked eyes, as shown in Fig. 19.

The workpiece was fixed on the worktable using a jaw vice as shown in Fig. 20, and the machining was performed as follows:

1. Side face A was milled first using a φ12 4-edge milling cutter to guarantee its straightness. Then, two holes were milled with a milling width of 5 μm using the same cutter, and one hole was machined without compensation (marked as "N" as shown in Fig. 19). One hole was machined with compensation (marked as "Y" as shown in Fig. 19). The *x*-axis was moved according to Table 3, and two holes were machined after each movement.
2. Side face B was milled by the same milling cutter to guarantee its straightness. Then, two holes were milled with a milling width of 5 μm, and one hole was machined without compensation (marked as "N" in Fig. 19). One

Table 3 Parameters of movement during machining

Axis	Number	Speed (mm/min)	Range (mm)	Time (min)
x	State 1	–	–	0
	State 2	6000	100–450	10
	State 3	8000	185–535	10
	State 4	10000	285–635	10
	State 5	0	600	15
y	State 1	–	–	0
	State 2	6000	−50 to −290	10
	State 3	8000	−130 to −370	12
	State 4	10000	−180 to −420	12
	State 5	0	−200	20
z	State 1	–	–	0
	State 2	6000	−302 to −47	10
	State 3	8000	−392 to −137	10
	State 4	10000	−442 to −187	15
	State 5	7000	−392 to −137	20

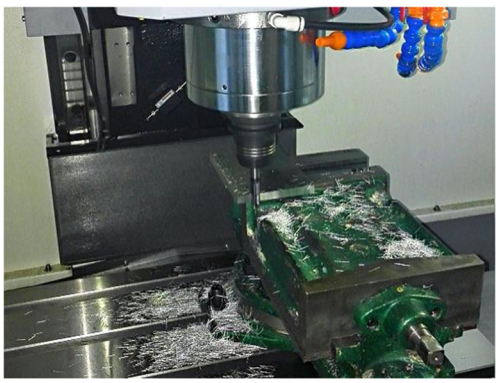

Fig. 20 Machining process

Fig. 21 Machining result

hole was machined with compensation (marked as "Y" in Fig. 19). The *y*-axis was moved according to Table 3, and two holes were machined after each movement.

3. The upper surface was milled by a φ20 2-edge milling cutter to guarantee its flatness. Then, two holes were milled with a milling depth of 5 μm using the same cutter on the upper side of the workpiece, and one hole was machined without compensation (marked as "N" in Fig. 19). One hole was machined with compensation (marked as "Y" in Fig. 19). The *z*-axis was moved according to Table 3, and two holes were machined after each movement.

Figure 21 shows the machined workpiece. Notably, the end of the cutter almost protruded; therefore, a mark of ring was obtained with a milling depth of 5 μm on the upper surface. Moreover, a machined trace occurred when the upper surface was machined; however, it did not affect the verification.

Figure 21 shows that the micron-level errors of the *x*-, *y*-, and *z*-axes can be easily observed by the naked eyes. From the machined holes before and after the compensation, even though the machine tool moved according to the changed states as shown in Table 3, the accuracy stability after the compensation were much better than those obtained before the compensation.

4 Conclusions

The sources and effects on the workpieces of the CTE of a servo axis were systematically investigated. The modeling and parameter optimization for TEE and TDE are presented. The simulation, experimental, and machining results show that the compensation effect of the suggested model is very good, and the accuracy stability after the compensation is much better than that obtained before the compensation. Moreover, the main advantage of the suggested model is its strong robustness. Therefore, high accuracy stability was obtained using this model in a nonconstant-temperature workshop, even though the machine tool moved randomly.

Acknowledgments The authors gratefully acknowledge the support of "High-Grade CNC Machine Tool and Basic Manufacturing Equipment" Science and Technology Major Project (2013ZX04011011). Moreover, the authors thank the anonymous referees and editor for their valuable comments and suggestions.

References

1. Ramesh R, Mannan MA, Poo AN (2000) Error compensation in machine tools—a review Part II: thermal errors. Int J Mach Tools Manuf 40:1257–84
2. Yang J, Shi H, Feng B, Zhao L, Ma C, Mei XS (2015) Thermal error modeling and compensation for a high-speed motorized spindle. Int J Adv Manuf Technol 77(5-8):1005–17
3. Yang J, Zhang DS, Mei XS, Zhao L, Ma C, Shi H (2015) Thermal error simulation and compensation in a jig-boring machine equipped with a dual-drive servo feed system. Proc Inst Mech Eng B J Eng Manuf 229(S1):43–63
4. Ni J (1997) CNC machine accuracy enhancement through real-time error compensation. J Manuf Sci E-T ASME 119:717–25
5. Yang J (1998) Error synthetic compensation technique and application for NC machine tools. Shanghai Jiao Tong University, Dissertation
6. Han ZY, Jin HY, Liu YL, Fu HY (2013) A review of geometric error modeling and error detection for CNC machine tool. Appl Mech Mater 303–306:627–31
7. Ozkan MT (2013) Experimental and artificial neural network study of heat formation values of drilling and boring operations on Al 7075 T6 workpiece. Indian J Eng Mater S 20:259–68
8. Yang J, Mei XS, Zhao L (2015) Thermal error compensation on a computer numerical control machine tool considering thermal tilt angles and cutting tool length. Proc Inst Mech Eng, B J Eng Manufacture 229(S1):78–97
9. Feng WL, Li ZH, Gu QY, Yang JG (2015) Thermally induced positioning error modeling and compensation based on thermal characteristic analysis. Int J Mach Tools Manuf 93:26–36
10. Fan K, Yang J, Yang L (2013) Orthogonal polynomials-based thermally induced spindle and geometric error modeling and compensation. Int J Adv Manuf Technol 65:1791–800
11. Wu CW, Tang CH, Chang CF, Shiao YS (2011) Thermal error compensation method for machine center. Int J Adv Manuf Technol 59:681–9
12. Zhang T, Ye WH, Liang RJ, Lou PH, Yang XL (2013) Temperature variable optimization for precision machine tool thermal error compensation on optimal threshold. Chin J Mech Eng 26:158–65
13. Pajor M, Zapłata J (2011) Compensation of thermal deformations of the feed screw in a CNC machine tool. Adv Manuf Sci Technol 35: 9–17
14. Zhang Y, Yang JG, Jiang H (2012) Machine tool thermal error modeling and prediction by grey neural network. Int J Adv Manuf Tech 59:1065–72
15. Horejs O, Mares M, Kohut P, Barta P, Hornych J (2010) Compensation of machine tool thermal errors based on transfer functions. MM Sci J 3:162–5
16. ISO 230-2:2006 (2006) Test code for machine tools – part 2: determination of accuracy and repeatability of positioning numerically controlled axes. International Standards Organization, Switzerland
17. Liu BJ (2013) Temperature field and thermal deformation of feed system on gantry machining center. Dissertation, Nanjing University of Aeronautics and Astronautics
18. Chen C, Qiu ZR, Li XF, Dong CJ, Zhang CY (2011) Temperature field model of ball screws used in servo systems. Optics and Precision Engineering 19:1151–8
19. Xiang ST, Yang JG, Zhang Y (2014) Modeling method for spindle thermal error based on mechanism analysis and thermal basic characteristics tests. J MECH ENG SCI 50:144–52
20. Zhang JZ, Chang HP (2009) Heat transfer. Science Press, Beijing
21. Holroyd G (2007) The modeling and correction of ball-screw geometric, thermal and load errors on CNC machine tools. Dissertation, The University of Huddersfield
22. Guo XG, Song XL, Cui YH (2013) Optimization on dynamic and fuel economy of electric vehicles based on Isight. Computer Aided Engineering 22:211–4
23. Wei W, Qu JY, Wu JY, Yan QD (2011) Research on optimization method for shift schedule of tracked vehicle with hydrodynamic–mechanical transmission. Acta Armamentarii 32:403–7